Journal of Materials Chemistry C

ROYAL SOCIETY OF CHEMISTRY

PAPER

View Article Online
View Journal | View Issue

Check for updates

Cite this: J. Mater. Chem. C, 2022, 10, 11686

Modeling the tunable thermal conductivity of intercalated layered materials with three-directional anisotropic phonon dispersion and relaxation times†

Chengjie Wang, [ab] Maogang He,[a] Xiangyang Liu[a] and Jonathan A. Malen*[bc]

Received 7th November 2021,
Accepted 13th July 2022

DOI: 10.1039/d1tc05369h

rsc.li/materials-c

An analytical model using three-directional anisotropic (TDA) dispersion and a novel anisotropic relaxation time (RT) relation for modeling the thermal conductivity (k) of intercalated layered materials is developed. The TDA dispersion eliminates the restriction of in-plane isotropy and is suitable for TDA materials such as black phosphorous. We compare calculations of k of bulk intercalated layered materials using the isotropic Debye dispersion and BvK dispersion with our TDA dispersion model, paired with both isotropic and anisotropic RTs. We find that calculated k values by the TDA dispersion model agree best with the experimental data. Furthermore, anisotropic RTs largely improve the performance of the Debye and BvK dispersion models whose average relative deviations for the in-plane k are reduced from 17.3% and 23.0% to 4.4% and 8.5%, respectively. Finally, thermal conductivity accumulation functions of intercalated MoS_2 and graphite are numerically calculated based on the TDA dispersion with anisotropic RTs. These models predict that intercalants cause increased contributions from phonons with shorter mean free paths, especially for in-plane thermal conductivity.

Published on 14 July 2022. Downloaded by Carnegie Mellon University on 1/10/2023 7:06:49 PM.

Introduction

Layered materials such as graphite, black phosphorus and transition-metal dichalcogenides (TMDs) comprise atomic layers with strong intra-layer covalent bonds stacked together by weak van der Waals (vdW) bonds.[1–4] The layered structure of these materials generates unique electronic, optical and thermal properties that are of great significance to energy storage, thermoelectric (TE) and optoelectronic devices.[5–8] Thermal conductivity is an important consideration in the design of these devices. For heat dissipation it should be maximized, but in TE devices its reduction enhances the thermoelectric figure of merit (ZT).[9–11]

Intercalation introduces guest ions or atoms into the vdW gaps of layered materials.[12] As a consequence, structural and compositional disorder between layers are induced, which can effectively tune the thermal conductivity of host materials and optimize the TE efficiency.[3] For example, the thermal conductivities of black phosphorus (black P) along the cross-plane, zigzag (ZZ) and armchair (AC) directions have been reduced by intercalating low-concentration Li^+ ions into the vdW gaps.[13] Liu *et al.* simultaneously reduced the thermal conductivity and enhanced the electrical transport properties of polycrystalline $SnSe_2$ through intercalation of Ag^+ ions, and achieved a peak ZT at 789 K along the cross-plane direction, which is 1.6 times larger than that of the original material.[14]

The tunability of thermal conductivity of intercalated layered materials has been previously studied by experiments and simulations.[1,3] An analytical model that offers insight into phonon transport and guides the tunability of thermal conductivity with intercalants is needed. Only Kang *et al.* analytically calculated the thermal conductivity of intercalated black P by the Callaway model[15] in which the Debye dispersion and relaxation time (RT) approximation to the Boltzmann transport equation[16] are used.[13] Although their calculated thermal conductivity agrees well with the experimental data at low intercalant concentrations, the Callaway model is based on the isotropic assumption despite the anisotropic thermal conductivity of layered materials. Despite Kang *et al.*'s meaningful work on black P, our extension of their model to evaluate the thermal conductivity of other intercalated layered materials such as MoS_2 and graphite, does not compare favorably with experiments.

In this work, we aim to improve upon two aspects of the Callaway model for intercalated layered materials. Firstly, the

[a] MOE Key Laboratory of Thermo-Fluid Science and Engineering, Xi'an Jiaotong University, Xi'an, Shaanxi, 710049, P. R. China
[b] Department of Mechanical Engineering, Carnegie Mellon University, Pittsburgh, PA, 15213, USA
[c] Department of Materials Science and Engineering, Carnegie Mellon University, Pittsburgh, PA, 15213, USA. E-mail: jonmalen@andrew.cmu.edu

† Electronic supplementary information (ESI) available. See DOI: https://doi.org/10.1039/d1tc05369h

This journal is © The Royal Society of Chemistry 2022

Published on 14 July 2022. Downloaded by Carnegie Mellon University on 1/10/2023 7:06:49 PM.

original Callaway model assumes isotropic dispersion which we herein replace with an anisotropic dispersion. Chen *et al.* proposed an anisotropic Debye dispersion by considering the first Brillouin zone (FBZ) boundary and the isoenergy surface as ellipsoids, by which the interfacial thermal conductance between graphite and metals, and minimum thermal conductivity of WSe_2 were successfully studied.[17,18] However, this dispersion model assumes that the in-plane phonon dispersion is isotropic which is incompatible for materials such as black P that exhibit three-directional anisotropy. Here we generalize the anisotropic Debye dispersion to accommodate three-direction anisotropy (*i.e.*, the TDA dispersion model). Second, the original RT does not consider the effect of intercalants on the atomic volume of the host materials, and we herein develop an anisotropic RT based on a virtual unit cell.[19] By combining our anisotropic RT and TDA dispersion model, we calculate the anisotropic thermal conductivity of intercalated layered materials such as MoS_2, graphite, black P, TiS_2 and $SnSe_2$. For comparison, the original and anisotropic RT are also combined with the Debye and BvK dispersion models.[20,21] Finally, we numerically calculate the anisotropic thermal conductivity accumulation function based on our TDA dispersion model for two typical intercalated layered materials (*i.e.* MoS_2 and graphite).

Analytical models

Callaway and BvKS models for thermal conductivity

There have been quite a few analytical models[22–26] for thermal conductivity, among which the Callaway[13] and BvKS models[20,21] are particularly classic. The Callaway model[13] is based on the Debye dispersion $\omega = v_s q$ where v_s is the sound speed and q is the wave vector. It calculates thermal conductivity as

$$k = \frac{k_B}{2\pi^2 v_s}\left(\frac{k_B}{\hbar}\right)^3 T^3 \int_0^{\theta_D/T} \frac{X^4 e^X}{(e^X-1)^2}\tau dX \quad (1)$$

where T, k_B, θ_D, and $\hbar$ are the temperature, Boltzmann constant, Debye temperature, and reduced Planck constant, respectively. The combined phonon relaxation time (RT), τ, will be explained later. The dimensionless parameter X is defined as $\hbar\omega/(k_B T)$ where ω is the phonon frequency.

The BvKS model uses the Born–von Karman (BvK) dispersion[20,21]

$$\omega = \omega_m \sin\left(\frac{\pi}{2}\frac{q}{q_m}\right) \quad (2)$$

where q_m is the cutoff wave vector based on the number density of primitive unit cells (N_p) $q_m = (6\pi^2 N_p)^{1/3}$ and ω_m is the maximum frequency $\omega_m = \frac{2}{\pi} v_s (6\pi^2 N_p)^{1/3}$.[20,21] It calculates thermal conductivity as

$$k = \frac{1}{3}\sum_p \frac{k_B^2 T q_m \omega_m}{\hbar\pi^3}\int_0^{\theta_m/T}\left[\arcsin\left(\frac{TX}{\theta_m}\right)\right]^2 \times \sqrt{1-\left(\frac{TX}{\theta_m}\right)^2}\frac{X^2 e^X}{(e^X-1)^2}\tau dX \quad (3)$$

where subscript p indexes the polarization of phonons and θ_m is defined as $\hbar\omega_m/k_B$.

The three-directional anisotropic dispersion model

The original anisotropic Debye model[17] expresses thermal conductivity as an integral over frequency

$$k_s = \sum_p \int_\omega \hbar\omega G_s(\omega)\frac{\partial f_{BE}}{\partial T}\tau d\omega \quad (4)$$

where subscript s means different directions in reciprocal space, G_s is the density of states weighted by the square of the s-direction projected velocity (referred to as the v^2DOS), which is defined in ref. 17 as

$$G_s(\omega) = \frac{1}{8\pi^3}\iint_{S_\omega}\frac{(\boldsymbol{v}_g\cdot\hat{\boldsymbol{s}})^2}{\|\boldsymbol{v}_g\|}dS_\omega \quad (5)$$

where $\boldsymbol{v}_g$ is the group velocity (vector), $\hat{\boldsymbol{s}}$ is the unit vector in s direction, dS_ω is an elemental area on an isoenergy surface within the FBZ (see Fig. 1). In what follows we have assumed a truncated linear dispersion relationship to evaluate G_s, but more accurate and complex representations of the dispersion (*e.g.* polynomial or trigonometric) could be used with this

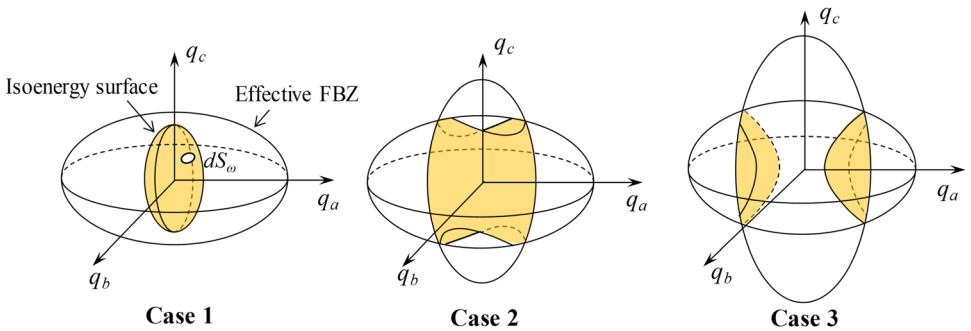

Fig. 1 The relationship between the isoenergy surface and effective FBZ for three frequency regimes. Case 1, $\omega < \omega_c$, all of the states on the isoenergy surface are allowed; Case 2, $\omega_c < \omega < \omega_b$, orange shading on the isoenergy surface is the allowed states; Case 3, $\omega_b < \omega < \omega_a$, orange shading on the isoenergy surface is the allowed states.

Published on 14 July 2022. Downloaded by Carnegie Mellon University on 1/10/2023 7:06:49 PM.

formalism by evaluating G_s from eqn (5), which is discussed in Section B of the ESI.†

The original anisotropic Debye model assumes isoenergy surface $\omega^2 = v_{ab}{}^2 q_{ab}{}^2 + v_c{}^2 q_c{}^2$ and FBZ $\frac{q_{ab}{}^2}{q_{ab,\mathrm{m}}{}^2} + \frac{q_c{}^2}{q_{c,\mathrm{m}}{}^2} = 1$ are ellipsoidal, where v_{ab} and v_c are the sound speeds, q_{ab} and q_c are the wave vectors, and $q_{ab,\mathrm{m}}$ and $q_{c,\mathrm{m}}$ are the cutoff wave vectors along the *ab* and *c* directions. In ref. 17 the in-plane *a* and *b* directions are equivalent, but we instead use a more general expression to produce a three-directional anisotropic model. Furthermore, Li *et al.* pointed out that the phonon dispersion in ref. 17 was linear and failed to capture the real group velocities of the phonons near the FBZ boundary.[9] We apply a truncated dispersion for longitudinal acoustic (LA) and transverse acoustic (TA) branches just as Li *et al.*[9] did, which sets the phonon group velocity to the sound speed except near the FBZ boundaries where it is zero. For the flexural (ZA) branch we do not use a piecewise group velocity for simplicity.[9]

With the above assumptions, equations describing the isoenergy surface and FBZ in our model are

$$\omega^2 = v_a{}^2 q_a{}^2 + v_b{}^2 q_b{}^2 + v_c{}^2 q_c{}^2 \tag{6}$$

$$\frac{q_a{}^2}{q_{a,\mathrm{eff}}{}^2} + \frac{q_b{}^2}{q_{b,\mathrm{eff}}{}^2} + \frac{q_c{}^2}{q_{c,\mathrm{eff}}{}^2} = 1 \tag{7}$$

where $q_{a,\mathrm{eff}}$, $q_{b,\mathrm{eff}}$ and $q_{c,\mathrm{eff}}$ are the effective cutoff wave vectors along the *a*, *b* and *c* directions, satisfying $\omega_a = v_a q_{a,\mathrm{eff}}$, $\omega_b = v_b q_{b,\mathrm{eff}}$ and $\omega_c = v_c q_{c,\mathrm{eff}}$ where ω_a, ω_b and ω_c are cutoff frequency. We define an effective FBZ within which phonons have nonzero group velocity,[9] so $q_{a,\mathrm{eff}}$, $q_{b,\mathrm{eff}}$ and $q_{c,\mathrm{eff}}$ represent the boundary of the effective FBZ. If we assume $\omega_a > \omega_b > \omega_c$, the area of the isoenergy surface S_ω within effective FBZ is defined by three cases that correspond to the conditions case 1: $\omega < \omega_c$, case 2: $\omega_c < \omega < \omega_b$ and case 3: $\omega_b < \omega < \omega_a$ as shown in Fig. 1. The shading area indicates the allowed phonon states in the effective FBZ.

Integrating $G_s(\omega)$ in eqn (5) over the shaded isoenergy surface for three cases, we get expressions for $G_s(\omega)$ in the *a*, *b* and *c* directions

$$G_a(\omega) = \begin{cases} \dfrac{v_a\omega^2}{6\pi^2 v_b v_c}, & 0 \le \omega < \omega_c \\ \dfrac{v_a\omega_c\omega}{4\pi^2 v_b v_c}\left[\dfrac{\omega_b{}^2-\omega^2}{\omega_b{}^2-\omega_c{}^2}\right]^{\frac{1}{2}} - \dfrac{v_a\omega_c{}^3}{12\pi^2 v_b v_c\omega}\left[\dfrac{\omega_b{}^2-\omega^2}{\omega_b{}^2-\omega_c{}^2}\right]^{\frac{3}{2}}, & \omega_c \le \omega < \omega_b \\ \dfrac{v_a\omega^2}{6\pi^2 v_b v_c} - \dfrac{v_a\omega_{\mathrm{D},a}{}^3}{6\pi^2 v_b v_c\omega}\left[\dfrac{\omega_b{}^2-\omega^2}{\omega_b{}^2-\omega_a{}^2}\right]^{\frac{3}{2}}, & \omega_b \le \omega \le \omega_a \end{cases} \tag{8}$$

$$G_b(\omega) = \begin{cases} \dfrac{v_b\omega^2}{6\pi^2 v_a v_c}, & 0 \le \omega < \omega_c \\ \dfrac{v_b\omega_c\omega}{4\pi^2 v_a v_c}\left[\dfrac{\omega_b{}^2-\omega^2}{\omega_b{}^2-\omega_c{}^2}\right]^{\frac{1}{2}} - \dfrac{v_b\omega_c{}^3}{12\pi^2 v_a v_c\omega}\left[\dfrac{\omega_b{}^2-\omega^2}{\omega_b{}^2-\omega_c{}^2}\right]^{\frac{3}{2}}, & \omega_c \le \omega < \omega_b \\ \dfrac{v_b\omega^2}{6\pi^2 v_a v_c} - \dfrac{v_b\omega_a\omega}{4\pi^2 v_a v_c}\left[\dfrac{\omega_b{}^2-\omega^2}{\omega_b{}^2-\omega_a{}^2}\right]^{\frac{1}{2}} + \dfrac{v_b\omega_a{}^3}{12\pi^2 v_a v_c\omega}\left[\dfrac{\omega_b{}^2-\omega^2}{\omega_b{}^2-\omega_a{}^2}\right]^{\frac{3}{2}}, & \omega_b \le \omega \le \omega_a \end{cases} \tag{9}$$

$$G_c(\omega) = \begin{cases} \dfrac{v_c\omega^2}{6\pi^2 v_a v_b}, & 0 \le \omega < \omega_c \\ \dfrac{v_c\omega_c{}^3}{6\pi^2 v_a v_b\omega}\left[\dfrac{\omega_b{}^2-\omega^2}{\omega_b{}^2-\omega_c{}^2}\right]^{\frac{3}{2}}, & \omega_c \le \omega < \omega_b \\ \dfrac{v_c\omega^2}{6\pi^2 v_a v_b} - \dfrac{v_c\omega_a\omega}{4\pi^2 v_a v_b}\left[\dfrac{\omega_b{}^2-\omega^2}{\omega_b{}^2-\omega_a{}^2}\right]^{\frac{1}{2}} + \dfrac{v_c\omega_a{}^3}{12\pi^2 v_a v_b\omega}\left[\dfrac{\omega_b{}^2-\omega^2}{\omega_b{}^2-\omega_a{}^2}\right]^{\frac{3}{2}}, & \omega_b \le \omega \le \omega_a \end{cases} \tag{10}$$

$G_a(\omega)$, $G_b(\omega)$ and $G_c(\omega)$ in the case 1 is the same as that in the ref. 17, but they are different for the other two cases. eqn (8)–(10) are derived under the premise that $\omega_a > \omega_b > \omega_c$, $G_a(\omega)$, $G_b(\omega)$ and $G_c(\omega)$ for the other situation ($\omega_a > \omega_c > \omega_b$) are similar. Substituting eqn (8)–(10) into eqn (4), the thermal conductivity along the three directions can be calculated. The detailed derivation of this TDA dispersion model is detailed in Section A of the ESI.† Notably, our TDA dispersion model reduces to the anisotropic Debye model[17] when the in-plane dispersion is isotropic and linear.

In the calculation by this model, we follow Chen *et al.*[17] and Li *et al.*[9] to decompose the longitudinal acoustic (LA) and transverse acoustic (TA) branches into TL1 and TL2 branches for black P based on the continuum elasticity theory.[27] Then we

 This journal is © The Royal Society of Chemistry 2022

Published on 14 July 2022. Downloaded by Carnegie Mellon University on 1/10/2023 7:06:49 PM.

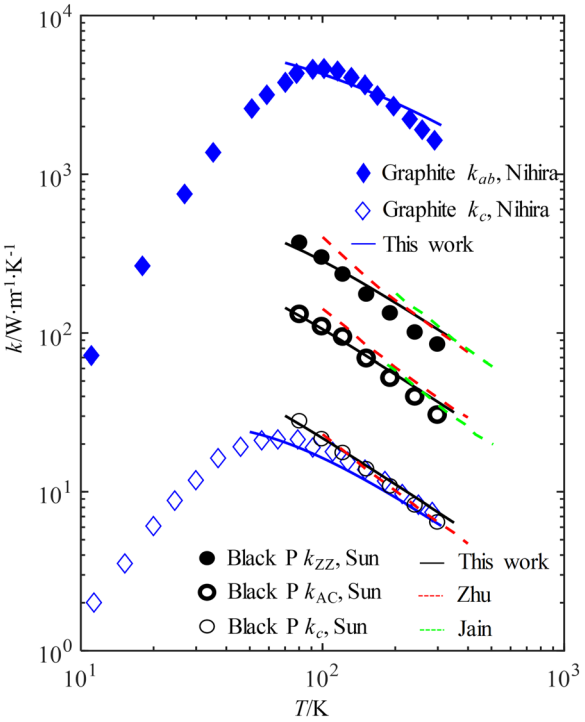

Fig. 2 Calculated thermal conductivity using our TDA dispersion model for black P and graphite, compared to the experimental data of black P by Sun *et al.*[2] and that of graphite by Nihira *et al.*,[28] in which the 1stP calculations for black P by Zhu *et al.*,[29] and phosphorene by Jain *et al.*[30] are also shown.

evaluate the anisotropic thermal conductivity of pure graphite and black P and compare the result to the experimental data by Sun *et al.*[2] and Nihira *et al.*,[28] and first-principle (1stP) calculation by Zhu *et al.*[29] and Jain *et al.*[30] Fig. 2 shows that the result of our model matches well with the experimental thermal conductivity for graphite and black P, indicating the validity our TDA model.

Relaxation time relations

The effective relaxation time τ is contributed by impurity scattering τ_i, anharmonic (Umklapp) phonon scattering τ_U, and boundary scattering τ_b, following the Matthiessen rule[15]

$$\tau^{-1} = \tau_i^{-1} + \tau_U^{-1} + \tau_b^{-1} = A\omega^4 + P\omega^2 T \exp\left(-\frac{C_U}{T}\right) + \frac{v}{L} \quad (11)$$

where L is the distance between boundaries and A, P and C_U are numerical coefficients. As the calculation is only performed at T = 300 K, we use one parameter B to represent $PT\exp(-C_U/T)$. For bulk materials at room temperature where L is large, τ_b^{-1} is much smaller than τ_i^{-1} and τ_U^{-1} and can be neglected. We have compared the relaxation times of pure MoS_2 and graphite in the in-plane direction using eqn (11) with published results from first-principles calculations[31,32] in Section E of the ESI.† Modifications to eqn (11) allow us to model intercalated materials. The impurity scattering coefficient A (A = 0 for pure materials) can be further expressed as two terms to describe mass disorder and lattice disorder contributing to impurity scattering[19,33,34]

$$A = \frac{V}{4\pi v_s^3}\left[\sum_i f_i\left(1-\frac{M_i}{M_{avg}}\right)^2 + \varepsilon\sum_i f_i\left(1-\frac{r_i}{r_{avg}}\right)^2\right] \quad (12)$$

where V is the atomic volume, f_i, M_i and r_i are the mole fraction, atomic mass and atomic radius of component i in the lattice, M_{avg} is the average atomic mass of all the components and r_{avg} is the average atomic radius. To describe lattice disorder, the phenomenological adjustable parameter, ε, is introduced and can be determined by experimental fitting. There is no lattice disorder when ε = 0, and ε is constrained to be larger than 0. Klemens built a formalism that can be used to relate ε to the Gruneisen parameter for cubic crystal structures, but its calculations with our model of layered materials deviated significantly from the experimental results.[16]

The atomic volume V in the mass disorder term in eqn (12) was originally defined as the V_u/n (where V_u is the volume of the unit cell and n is the number of atoms in the unit cell)[16] for elemental crystals. In order to get V of a semiconductor alloy, Abeles used the virtual crystal approach and computed V by $V = \delta^3 = (\Sigma f_i\delta_i)^3$ (where f_i and δ_i are the concentration and cube root of the atomic volume of component i of the alloy respectively).[19] In order to consider the effect of the intercalants on the structure of the host lattice, we attempt to apply Abeles's approach to the intercalated layered materials and regard the host atoms and intercalants as two components in the lattice, just like two phases in the alloy. We define the cube root of the atomic volume of the intercalated materials as the atomic distance d, so that $V = d^3$ and d is expressed as

$$d = f_g d_g + f_h d_h \quad (13)$$

where the subscripts g and h signify guest (intercalants) and host atoms. For the anisotropic materials in this paper, the atomic distance d_h along different directions varies, and is related to the lattice constants (a_0, b_0, and c_0). By assuming the atoms distribute randomly in the unit cell, d_h along the a, b and c directions are $a_0/\sqrt[3]{n}$, $b_0/\sqrt[3]{n}$ and $c_0/\sqrt[3]{n}$. If the material is in-plane isotropic such as graphite, d_h should be $\sqrt{S_{ab}}/\sqrt[3]{n}$ ($\sqrt{S_{ab}}$ is the in-plane area of the unit cell) along the in-plane direction and $c_0/\sqrt[3]{n}$ along the cross-plane direction. Substituting d_h into the eqn (13), the effective atomic volume V_{eff} along the in-plane and cross-plane directions can be obtained. We further refer to the relaxation time defined by eqn (11)–(13) with this V_{eff} as the directionally dependent relaxation time (anisotropic RT).

Results and discussion

Calculation of the thermal conductivities of intercalated layered materials

Intercalants have been experimentally added to several layered materials,[1,3,5,13,14,35–45] most of which exhibit reduced thermal conductivity with some important exceptions. Pawula *et al.* reported that intercalated Fe atoms enhance the cross-plane thermal conductivity of TiS_2 slightly because Fe may create

Published on 14 July 2022. Downloaded by Carnegie Mellon University on 1/10/2023 7:06:49 PM.

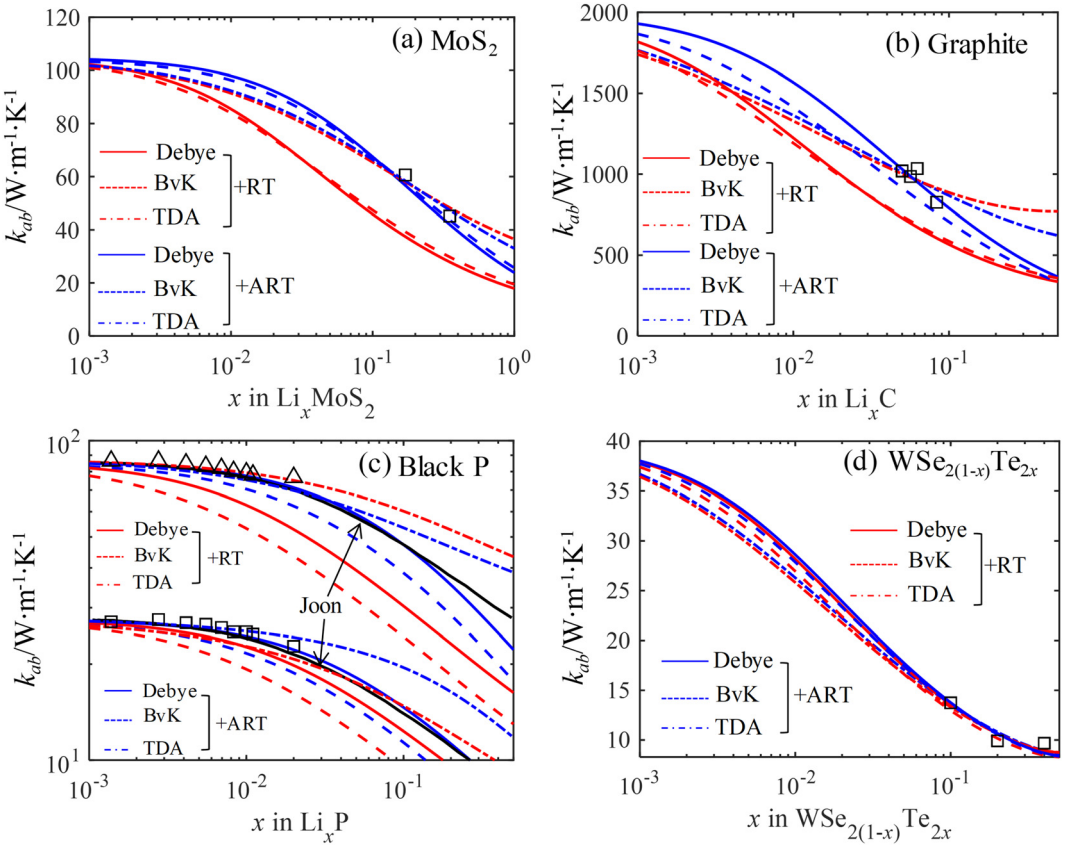

Fig. 3 Calculated in-plane thermal conductivity of (a) MoS_2, (b) graphite, (c) BP and (d) $WSe_{2(1-x)}Te_{2x}$ by Debye, BvK and TDA dispersion models combined with the original and anisotropic RT at different intercalant concentrations x, compared to the experimental data (square) of MoS_2 by Zhu *et al.*,[3] graphite by Wei *et al.*,[5] black P by Kang *et al.*[13] and $WSe_{2(1-x)}S_{2x}$ by Qian *et al.*,[46] in which ART represents anisotropic RT. For black P, square and triangle represent the thermal conductivity along armchair (AC) and zigzag (ZZ) directions, respectively.

phonon conduction paths instead of phonon scattering sources in the lattice.[44] Zhu *et al.* showed that the thermal conductivity of Li_xMoS_2 decreases at small concentrations but increases with greater concentrations of intercalated Li atoms.[3] This increased thermal conductivity is attributed to a phase transition that occurs with high Li concentration. Since our model describes the intercalated thermal conductivity reductions through increased phonon scattering, we will not choose these exceptions as test cases. The following data were considered here: anisotropic thermal conductivity data of Li_xMoS_2 (synthetized by electrochemical intercalation, measured by time-domain thermoreflectance (TDTR)),[3] Li_xP (black phosphorus, synthetized by electrochemical intercalation, measured by TDTR),[13] Li_xC (graphite, molecular dynamics simulation),[5] $WSe_{2(1-x)}Te_{2x}$ (layered-material alloy with disorder which is similar to the intercalated material, synthesized by chemical vapor transport, measured by TDTR),[46] Cu_xTiS_2 (synthetized by melting combined with spark plasma sintering, measured by laser flash system)[35] and $SnSe_2Cl_x$ (synthetized by melting-quenching combined with spark plasma sintering, measured by laser flash).[36] For Cu_xTiS_2 and $SnSe_2Cl_x$, only the cross-plane thermal conductivity data are available.

We compare the thermal conductivities of the selected materials at T = 300 K using the Debye, BvK and TDA dispersion models in Fig. 3 (in-plane) and Fig. 4 (cross-plane), in which both the original and anisotropic RT are considered. The optimized fitting parameters and input parameters in the calculation are listed in Table 1 and Table S1 in Section D of the ESI,† respectively. Fig. 3 shows that the TDA dispersion model agrees best with the experimental data whether the original or anisotropic RT is used. With the original RT, Debye and BvK dispersion models underestimate the in-plane thermal conductivities of MoS_2, black P and graphite, attributed to the large impurity scattering coefficient A in the calculation, which is reflected by the fact that the fitting parameter ε_{ab} is zero as shown in Table 1. However, this underestimation is improved by our anisotropic RT which decrease A along the in-plane direction because V_{eff} along this direction is smaller than the original V. The calculated cross-plane thermal conductivities by three thermal conductivity models are all in a good agreement with the experimental data as shown in Fig. 4.

A parity plot of the experimental and calculated thermal conductivities using original and anisotropic RT are displayed in Fig. 5. It shows that our anisotropic RT enhances the accuracy of the Debye and BvK dispersion models when modeling the in-plane thermal conductivities of MoS_2, BP and graphite. In order to quantify the improvement comprehensively with the anisotropic RT, the average relative deviations (ARDs) and root mean square errors (RMSEs) between the

 This journal is © The Royal Society of Chemistry 2022

Published on 14 July 2022. Downloaded by Carnegie Mellon University on 1/10/2023 7:06:49 PM.

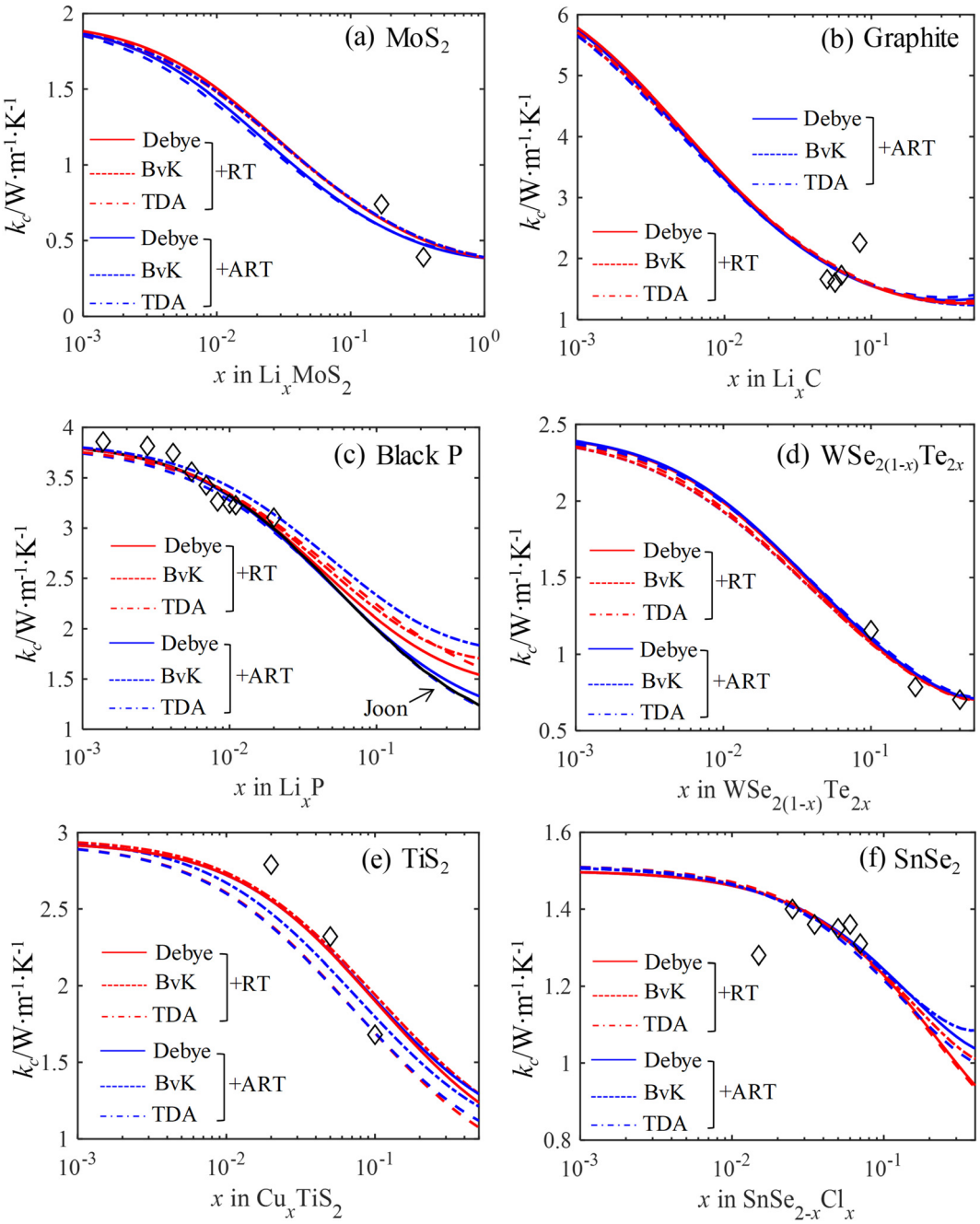

Fig. 4 Calculated cross-plane thermal conductivity of intercalated (a) MoS_2, (b) graphite, (c) black P, (d) $WSe_{2(1-x)}Te_{2x}$, (e) TiS_2 and (f) $SnSe_2$ by Debye, BvK and TDA dispersion models combined with the original and anisotropic RT at different intercalant concentrations x, compared to the experimental data (diamond) of MoS_2 by Zhu *et al.*,[3] graphite by Wei *et al.*,[5] black P by Kang *et al.*,[13] $WSe_{2(1-x)}S_{2x}$ by Qian *et al.*,[46] TiS_2 by Guilmeau *et al.*[35] and $SnSe_2$ by Shu *et al.*,[36] in which ART represents anisotropic RT.

experimental and calculated thermal conductivity are obtained in Table 2, whose equations are

$$\mathrm{ARD} = \frac{1}{N}\sum_{i=1}^{N}\left(\left|k_{i,\mathrm{cal}} - k_{i,\mathrm{exp}}\right|/k_{i,\mathrm{exp}}\right) \quad (14)$$

$$\mathrm{RMSE} = \sqrt{\frac{1}{N}\sum_{i=1}^{N}\left(k_{i,\mathrm{cal}} - k_{i,\mathrm{exp}}\right)^2} \quad (15)$$

where N is the number of thermal conductivity data, k_{exp} and k_{cal} are the experimental and calculated thermal conductivity. ARD is a relative parameter and RMSE is an absolute one. With the anisotropic RT, the ARDs for the in-plane thermal conductivity by Debye and BvK dispersion models decrease from 17.3% and 23.0% to 4.4% and 8.5%, respectively and the RMSEs using these two models decrease from 103.8 W m^{-1} K^{-1} and 108.9 W m^{-1} K^{-1} to 16.7 W m^{-1} K^{-1} and 17.4 W m^{-1} K^{-1}. The high accuracy of the TDA dispersion model is not improved. For the cross-plane

Published on 14 July 2022. Downloaded by Carnegie Mellon University on 1/10/2023 7:06:49 PM.

Table 1 Fitting parameters for Li_xMoS_2, Li_xP (black phosphorus), Li_xC (graphite), $WSe_{2(1-x)}Te_{2x}$, Cu_xTiS_2 and $SnSe_{2-x}Cl_x$ in the calculation by Debye, BvK and TDA dispersion models combined with the original and anisotropic RT, respectively

Material	Dispersion model	RT	B_{ab} (10^{-16} s)	B_c (10^{-15} s)	ε_{ab}	ε_c
Li_xMoS_2	Debye	Original	0.48	1.43	0	347
		Anisotropic	0.48	1.43	0	20
	BvK	Original	0.50	0.61	0	857
		Anisotropic	0.50	0.61	0	61
	TDA	Original	0.67	0.96	4	106
		Anisotropic	0.67	0.96	11	6
Li_xC	Debye	Original	0.028	0.45	0	19
		Anisotropic	0.028	0.45	0	2
	BvK	Original	0.025	0.32	0	24
		Anisotropic	0.025	0.32	0	3
	TDA	Original	0.070	0.143	0.8	2.9
		Anisotropic	0.070	0.143	1.3	0.3
Li_xP	Debye	Original	0.42(ZZ), 1.59(AC)	0.51	0	8
		Anisotropic	0.42(ZZ), 1.59(AC)	0.51	0	0
	BvK	Original	0.61(ZZ), 1.92(AC)	0.81	0	3
		Anisotropic	0.61(ZZ), 1.92(AC)	0.81	0	0
	TDA	Original	1.36(ZZ), 1.05(AC)	1.39	0	28
		Anisotropic	1.36(ZZ), 1.05(AC)	1.39	3(ZZ) 0(AC)	3
$WSe_{2(1-x)}Te_{2x}$	Debye	Original	2.20	0.81	32	556
		Anisotropic	2.20	0.81	156	22
	BvK	Original	1.26	0.46	82	1020
		Anisotropic	1.26	0.46	327	45
	TDA	Original	1.13	0.4	306	388
		Anisotropic	1.13	0.4	1224	10
Cu_xTiS_2	Debye	Original		0.73		214
		Anisotropic		0.73		61
	BvK	Original		0.87		159
		Anisotropic		0.87		45
	TDA	Original		0.94		70
		Anisotropic		0.94		25
$SnSe_{2-x}Cl_x$	Debye	Original		1.46		71
		Anisotropic		1.46		20
	BvK	Original		1.59		114
		Anisotropic		1.59		20
	TDA	Original		1.60		28
		Anisotropic		1.60		6

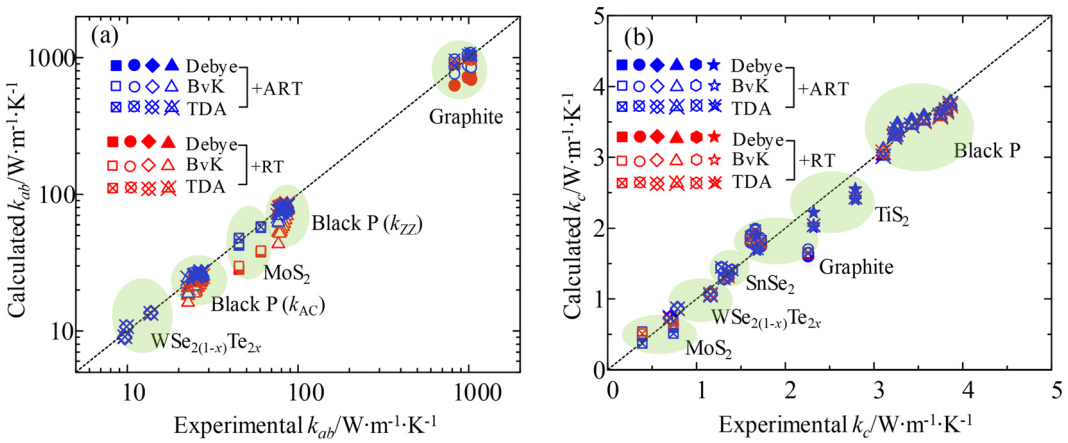

Fig. 5 Parity plot of the experimental and calculated thermal conductivity of intercalated MoS_2, black P, graphite, $WSe_{2(1-x)}Te_{2x}$, TiS_2 and $SnSe_2$ by Debye, BvK and TDA dispersion models, in which ART represents anisotropic RT. (a) In-plane thermal conductivity; (b) cross-plane thermal conductivity.

thermal conductivity, ARDs and RMSEs for three dispersion models using anisotropic RT (7.3% and 0.2 W m^{-1} K^{-1}) are almost the same as that using original RT (7.2% and 0.2 W m^{-1} K^{-1}).

It is worth noting that the thermal conductivity of black P along the ZZ and AC directions calculated by Callaway model (Debye dispersion + original RT) in our paper differs from that in ref. 13 as the black line shows in Fig. 3. Kang *et al.*[13] used V_u to calculate A in eqn (12), but we used V like Klemens,[16] Abeles,[19] Zhou *et al.*[33] and Yang *et al.*[34] Kang *et al.* does not provide the input parameters used in their calculations,[13] so we

 This journal is © The Royal Society of Chemistry 2022

Published on 14 July 2022. Downloaded by Carnegie Mellon University on 1/10/2023 7:06:49 PM.

Table 2 ARDs and RMSEs of three dispersion models (Debye, BvK and TDA models) in the calculation combined with original and anisotropic RT, respectively

	ARD (%)				RMSE (W m^{-1} K^{-1})			
	In-plane		Cross-plane		In-plane		Cross-plane	
Dispersion model	Original RT	Anisotropic RT	Original RT	Anisotropic RT	Original RT	Anisotropic RT	Original RT	Anisotropic RT
Debye	17.3	4.4	7.2	7.1	103.8	16.7	0.2	0.2
BvK	23.0	8.5	7.1	7.5	108.9	17.4	0.2	0.2
TDA	5.0	4.6	7.4	7.4	22.4	22.5	0.2	0.2

are unable to further confirm the source of this discrepancy. Here we present our input parameters in Table S1 in Section D of the ESI,† which are extracted from ref. 9 (MoS_2 and graphite), ref. 47 (black P), ref. 48 ($WSe_{2(1-x)}Te_{2x}$), ref. 49 (TiS_2) and ref. 50 ($SnSe_2$).

Table 1 shows that ε fitted using the Debye and BvK dispersion models are zero for the in-plane direction but large along the cross-plane direciton (except for $WSe_{2(1-x)}Te_{2x}$), suggesting that lattice distortion only influences phonon transport in the cross-plane direction. This result is different from that of our TDA dispersion model, which shows that lattice distortion influences phonon transport in both directions. It also shows that anisotropic RT has the potential to mediate the degree of lattice disorder for both direcitons which increases ε_{ab} and decreases ε_c. ε for black P, MoS_2 and graphite are genearlly less than that of $WSe_{2(1-x)}Te_{2x}$ alloy, indicating that large atomic mass difference between Li^+ ion and host atoms (P, Mo and C) provides the major contribution to the impurity scattering.[13]

Thermal conductivity accumulation function

To study the contributions of the mean free path (MFP) of phonons to the bulk thermal conductivity (k_{bulk}), the cumulative MFP-dependent thermal conductivity accumulation function for layered material is derived. For isotropic materials, k_{bulk} can be expressed as a function of MFP Λ, where $\Lambda = v_g\tau$[51,52] and

$$k_{bulk} = \int_0^\infty k_\Lambda d\Lambda \quad (16)$$

where k_Λ is the thermal conductivity per unit MFP. By restricting the upper limit of integration and normalizing by k_{bulk}, the normalized accumulation function[21] is defined as

$$\alpha(\Lambda^*) = \frac{1}{k_{bulk}}\int_0^{\Lambda^*} k_\Lambda d\Lambda \quad (17)$$

which represents the fractional contribution of phonons with MFPs less than Λ^* to the total thermal conductivity. It is possible to derive an explicit expression as a function of MFP for the Debye and BvK dispersion models, however, an analytical expression as a function of MFP cannot be derived for the TDA dispersion model. Herein we numerically calculate the thermal conductivity accumulation function using TDA dispersion model, which is detailed in Section C of the ESI.†

Since MoS_2 and graphite are the most widely studied layered materials, we calculate their normalized accumulation function at T = 300 K with Debye, BvK and TDA dispersion models. Comparison between the calculated result and first-principle (1stP) calculations[53–56] is presented in Fig. 6 for MoS_2 and Fig. 7 for graphite. The distribution of α by three dispersion models spans a broader range of phonon MFPs than that by 1stP[53] for MoS_2, in which phonons with MFP less than 10^3 nm contribute 96% to k_{ab} for 1stP but 70–80% for the three models considered here. Predictions of α the by TDA dispersion model matches best with the 1stP result, especially at the short MFP. For graphite, the normalized accumulation function for the in-plane thermal conductivity α_{ab} by the TDA dispersion model agrees well with the 1stP calculation by Lindsay[55] at short MFP, but become closer to the 1stP result of Kuang[56] at long MFP, see from Fig. 7a. There are no 1stP calculation for the cross-plane thermal conductivity of graphite. Result by MD (molecular dynamics)[57] is

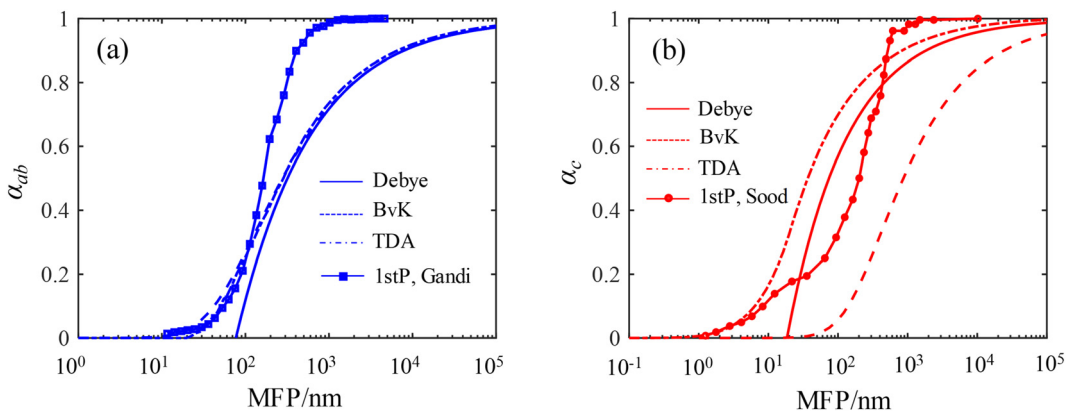

Fig. 6 Normalized accumulation function for the (a) in-plane and (b) cross-plane thermal conductivity of pure MoS_2 by Debye, BvK and TDA dispersion models, compared to the result of Gandi *et al.*[53] and Sood *et al.*[54] by 1stP.

Published on 14 July 2022. Downloaded by Carnegie Mellon University on 1/10/2023 7:06:49 PM.

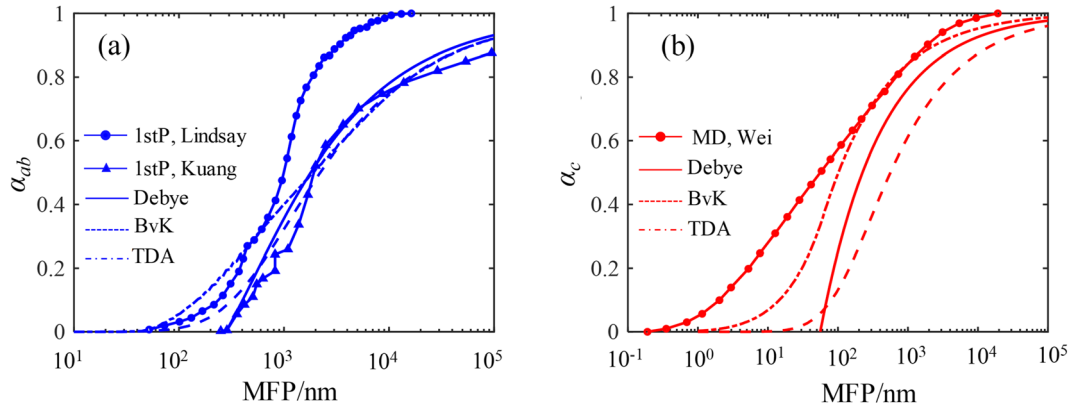

Fig. 7 Normalized thermal conductivity accumulation function for the (a) in-plane and (b) cross-plane thermal conductivity of pure graphite by Debye, BvK and TDA dispersion models, compared to result of Lindsay *et al.*[55] and Kuang *et al.*[56] by 1stP, and Wei *et al.*[57] by MD.

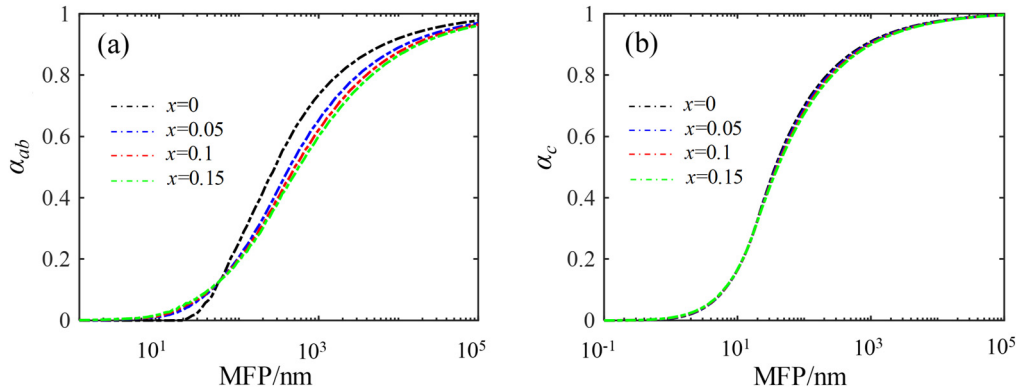

Fig. 8 Normalized accumulation function for the (a) in-plane and (b) cross-plane thermal conductivity of Li_xMoS_2 by the TDA dispersion model.

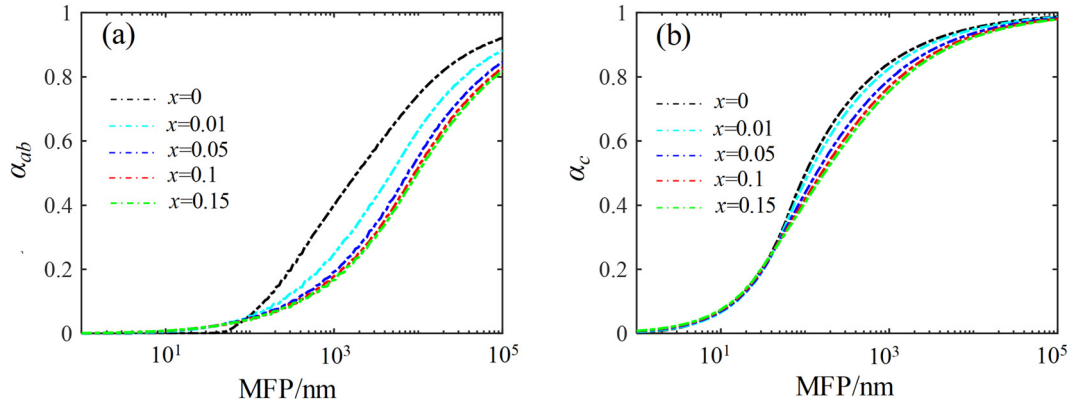

Fig. 9 Normalized accumulation function for the (a) in-plane and (b) cross-plane thermal conductivity of Li_xC (graphite) by the TDA dispersion model.

presented in Fig. 7b, which differ a lot from our result at short MFP, but agree well with ours at long MFP.

To exemplify how the normalized thermal conductivity accumulation function change as a function of intercalant concentration, we show that of Li_xMoS_2 and Li_xC (graphite) at T = 300 K with TDA dispersion model in Fig. 8 and 9. This calculation suggests that intercalants cause α_{ab} of MoS_2 and graphite to span a broader range of phonon MFPs. Shorter MFP begin to contribute to the thermal conductivity, and long MFP contributions gradually decrease. The intercalants do not affect α_c as drastically as α_{ab} and only slowly reduce the contribution of phonons with long MFP to the cross-plane thermal

 This journal is © The Royal Society of Chemistry 2022

Published on 14 July 2022. Downloaded by Carnegie Mellon University on 1/10/2023 7:06:49 PM.

conductivity of graphite and have negligible effect on α_c of MoS_2 when x is less than 0.15. Overall, the intercalants have a larger impact on α of graphite compared to MoS_2, because the volume and atomic mass of the graphite lattice is much smaller than that of MoS_2 and the intercalants cause greater disorder to the graphite lattice.

Conclusion

Here we derive a three-directional anisotropic dispersion model based on the work of Chen *et al.*[17] and pair it with anisotropic relaxation time to understand the thermal conductivity of intercalated layered materials. Debye, BvK and our TDA dispersion models are compared using both original and anisotropic RT. The TDA dispersion model performs best and the anisotropic RT improves the accuracy of calculations using Debye and BvK dispersion models whose average relative deviations decrease from 17.3% and 23.0% to 4.4% and 8.5%, and root mean square errors decrease from 103.8 W m^{-1} K^{-1} and 108.9 W m^{-1} K^{-1} to 16.7 W m^{-1} K^{-1} and 17.4 W m^{-1} K^{-1}, as compared to the original RT. The normalized thermal conductivity accumulation functions based on the TDA dispersion model for pure and intercalated MoS_2 and graphite are numerically calculated. The intercalants cause larger in-plane than cross-plane changes to thermal conductivity accumulation where phonons with shorter MFPs contribute more significantly, while phonons with long MFPs contribute less.

Author contributions

Chengjie Wang: conceptualization, methodology, software, writing – original draft. Maogang He: supervision, funding acquisition, validation. Xiangyang Liu: conceptualization, resources. Jonathan A. Malen: validation, writing – review & editing, supervision, funding acquisition.

Conflicts of interest

There are no conflicts of interest to declare.

Acknowledgements

Jonathan A. Malen is thankful for support provided by the NSF ENG ECCS Award (No. 1901972). Chengjie Wang, Maogang He and Xiangyang Liu are thankful for support provided by the Foundation for Innovative Research Groups of the National Natural Science Foundation of China (No. 51721004) and China Scholarship Council (No. 201906280332).

References

1 X. Qian, X. Gu, M. S. Dresselhaus and R. Yang, *J. Phys. Chem. Lett.*, 2016, **7**, 4744–4750.
2 B. Sun, X. Gu, Q. Zeng, X. Huang, Y. Yan, Z. Liu, R. Yang and Y. K. Koh, *Adv. Mater.*, 2017, **29**, 1603297.
3 G. Zhu, J. Liu, Q. Zheng, R. Zhang, D. Li, D. Banerjee and D. G. Cahill, *Nat. Commun.*, 2016, **7**, 1–9.
4 K. Khan, A. K. Tareen, M. Aslam, R. Wang, Y. Zhang, A. Mahmood, Z. Ouyang, H. Zhang and Z. Guo, *J. Mater. Chem. C*, 2020, **8**, 387–440.
5 Z. Wei, F. Yang, K. Bi, J. Yang and Y. Chen, *J. Phys. Chem. C*, 2018, **122**, 1447–1455.
6 A. Kretinin, Y. Cao, J. Tu, G. Yu, R. Jalil, K. Novoselov, S. Haigh, A. Gholinia, A. Mishchenko and M. Lozada, *Nano Lett.*, 2014, **14**, 3270–3276.
7 X. Zhang, L. Hou, A. Ciesielski and P. Samorì, *Adv. Energy Mater.*, 2016, **6**, 1600671.
8 Y. Kobayashi, S. Sasaki, S. Mori, H. Hibino, Z. Liu, K. Watanabe, T. Taniguchi, K. Suenaga, Y. Maniwa and Y. Miyata, *ACS Nano*, 2015, **9**, 4056–4063.
9 H. Li, W. Zheng and Y. K. Koh, *Phys. Rev. Mater.*, 2018, **2**, 123802.
10 X. Wang, Y. Hong, D. Ma and J. Zhang, *J. Mater. Chem. C*, 2017, **5**, 5119–5127.
11 H. H. Huang, X. Fan, D. J. Singh and W. T. Zheng, *J. Mater. Chem. C*, 2019, **7**, 10652–10662.
12 M. Takeuchi, H. Imai and Y. Oaki, *J. Mater. Chem. C*, 2017, **5**, 8250–8255.
13 J. S. Kang, M. Ke and Y. Hu, *Nano Lett.*, 2017, **17**, 1431–1438.
14 C. Liu, Z. Huang, D. Wang, X. Wang, L. Miao, X. Wang, S. Wu, N. Toyama, T. Asaka and J. Chen, *J. Mater. Chem. A*, 2019, **7**, 9761–9772.
15 J. Callaway, *Phys. Rev.*, 1959, **113**, 1046–1051.
16 P. Klemens, *Proc. Phys. Soc., London, Sect. A*, 1955, **68**, 1113–1128.
17 Z. Chen, Z. Wei, Y. Chen and C. Dames, *Phys. Rev. B: Condens. Matter Mater. Phys.*, 2013, **87**, 125426.
18 Z. Chen and C. Dames, *Appl. Phys. Lett.*, 2015, **107**, 193104.
19 B. Abeles, *Phys. Rev.*, 1963, **131**, 1906–1911.
20 C. Dames and G. Chen, *J. Appl. Phys.*, 2004, **95**, 682–693.
21 F. Yang and C. Dames, *Phys. Rev. B: Condens. Matter Mater. Phys.*, 2013, **87**, 035437.
22 Y. Guo, D. Jou and M. Wang, *Phys. Rev. B*, 2018, **98**, 104304.
23 C. De Tomas, A. Cantarero, A. Lopeandia and F. Alvarez, *J. Appl. Phys.*, 2014, **115**, 164314.
24 P. B. Allen, *Phys. Rev. B: Condens. Matter Mater. Phys.*, 2013, **88**, 144302.
25 Z. Chen, X. Zhang, S. Lin, L. Chen and Y. Pei, *Natl. Sci. Rev.*, 2018, **5**, 888–894.
26 E. S. Toberer, A. Zevalkink and G. J. Snyder, *J. Mater. Chem.*, 2011, **21**, 15843–15852.
27 B. A. Auld, *Acoustic fields and waves in solids*, Ripol Classic, 1973.
28 T. Nihira and T. Iwata, *Jpn. J. Appl. Phys.*, 1975, **14**, 1099–1104.
29 J. Zhu, H. Park, J. Y. Chen, X. Gu, H. Zhang, S. Karthikeyan, N. Wendel, S. A. Campbell, M. Dawber and X. Du, *Adv. Electron. Mater.*, 2016, **2**, 1600040.
30 A. Jain and A. J. McGaughey, *Sci. Rep.*, 2015, **5**, 1–5.
31 L. Zhu, T. Zhang, Z. Sun, J. Li, G. Chen and S. A. Yang, *Nanotechnology*, 2015, **26**, 465707.

Published on 14 July 2022. Downloaded by Carnegie Mellon University on 1/10/2023 7:06:49 PM.

32 A. Taheri, C. Da Silva and C. H. Amon, *J. Appl. Phys.*, 2018, **123**, 215105.
33 Z. Zhou, C. Uher, A. Jewell and T. Caillat, *Phys. Rev. B: Condens. Matter Mater. Phys.*, 2005, **71**, 235209.
34 J. Yang, G. Meisner and L. Chen, *Appl. Phys. Lett.*, 2004, **85**, 1140–1142.
35 E. Guilmeau, Y. Bréard and A. Maignan, *Appl. Phys. Lett.*, 2011, **99**, 052107.
36 Y. Shu, X. Su, H. Xie, G. Zheng, W. Liu, Y. Yan, T. Luo, X. Yang, D. Yang and C. Uher, *ACS Appl. Mater. Interfaces*, 2018, **10**, 15793–15802.
37 L. Ruan, H. Zhao, D. Li, S. Jin, S. Li, L. Gu and J. Liang, *J. Electron. Mater.*, 2016, **45**, 2926–2934.
38 S. Chen, A. Sood, E. Pop, K. E. Goodson and D. Donadio, *2D Mater.*, 2019, **6**, 025033.
39 D. Li, X. Qin and Y. Gu, *Mater. Res. Bull.*, 2006, **41**, 282–290.
40 R. Bhatt, S. Bhattacharya, M. Patel, R. Basu, A. Singh, C. Sürger, M. Navaneethan, Y. Hayakawa, D. Aswal and S. Gupta, *J. Appl. Phys.*, 2013, **114**, 114509.
41 T. C. Holgate, Y. Liu, D. Hitchcock, T. M. Tritt and J. He, *J. Electron. Mater.*, 2013, **42**, 1751–1755.
42 R. Nunna, F. Gascoin and E. Guilmeau, *J. Alloys Compd.*, 2015, **634**, 32–36.
43 C. Wan, X. Gu, F. Dang, T. Itoh, Y. Wang, H. Sasaki, M. Kondo, K. Koga, K. Yabuki and G. J. Snyder, *Nat. Mater.*, 2015, **14**, 622–627.
44 F. Pawula, R. Daou, S. Hébert, O. Lebedev, A. Maignan, A. Subedi, Y. Kakefuda, N. Kawamoto, T. Baba and T. Mori, *Phys. Rev. B*, 2019, **99**, 085422.
45 D. Li, X. Qin, J. Zhang and H. Li, *Phys. Lett. A*, 2006, **348**, 379–385.
46 X. Qian, P. Jiang, P. Yu, X. Gu, Z. Liu and R. Yang, *Appl. Phys. Lett.*, 2018, **112**, 241901.
47 C. Kaneta, H. Katayama-Yoshida and A. Morita, *J. Phys. Soc. Jpn.*, 1986, **55**, 1213–1223.
48 D. O. Lindroth and P. Erhart, *Phys. Rev. B*, 2016, **94**, 115205.
49 C. Wan, Y. Wang, N. Wang, W. Norimatsu, M. Kusunoki and K. Koumoto, *J. Electron. Mater.*, 2011, **40**, 1271–1280.
50 Y. Wu, W. Li, A. Faghaninia, Z. Chen, J. Li, X. Zhang, B. Gao, S. Lin, B. Zhou and A. Jain, *Mater. Today Phys.*, 2017, **3**, 127–136.
51 J. P. Freedman, J. H. Leach, E. A. Preble, Z. Sitar, R. F. Davis and J. A. Malen, *Sci. Rep.*, 2013, **3**, 1–6.
52 K. T. Regner, J. P. Freedman and J. A. Malen, *Nanoscale Microscale Thermophys. Eng.*, 2015, **19**, 183–205.
53 A. N. Gandi and U. Schwingenschlögl, *Europhys. Lett.*, 2016, **113**, 36002.
54 A. Sood, F. Xiong, S. Chen, R. Cheaito, F. Lian, M. Asheghi, Y. Cui, D. Donadio, K. E. Goodson and E. Pop, *Nano Lett.*, 2019, **19**, 2434–2442.
55 L. Lindsay, W. Li, J. Carrete, N. Mingo, D. Broido and T. Reinecke, *Phys. Rev. B: Condens. Matter Mater. Phys.*, 2014, **89**, 155426.
56 Y. Kuang, L. Lindsay, S. Shi, X. Wang and B. Huang, *Int. J. Heat Mass Transfer*, 2016, **101**, 772–778.
57 Z. Wei, J. Yang, W. Chen, K. Bi, D. Li and Y. Chen, *Appl. Phys. Lett.*, 2014, **104**, 081903.

 This journal is © The Royal Society of Chemistry 2022